



Short Communication

Effect of HfO₂ dispersoids on the microstructure of a Ni-Cr-Al-Ti superalloy processed by laser-based powder-bed fusionAnthony De Luca^{a,1}, Christoph Kenel^{b,1,2}, David C. Dunand^b, Christian Leinenbach^{a,c,*}^a Empa – Swiss Federal Laboratories for Materials Science and Technology, Überlandstrasse 129, Dübendorf 8600, Switzerland^b Department of Materials Science and Engineering, Northwestern University, 2220 Campus Drive, Evanston, IL 60208, United States^c Laboratory for Photonic Materials and Characterization, École Polytechnique Fédérale de Lausanne, Lausanne 1015, Switzerland

ARTICLE INFO

Keywords:

Additive manufacturing
Laser powder bed fusion
Nickel superalloy
Oxide dispersion strengthening

ABSTRACT

The effects of 1 wt% HfO₂ nano-dispersoid addition on the microstructure of a high- γ' Ni-8.5Cr-5.5Al-1Ti (wt%) model superalloy are investigated after manufacturing via laser-based powder-bed fusion (PBF-LB). Despite their very high melting point, HfO₂ dispersoids are not fully stable during their short stay in the melt pool. At the nanoscale, the superalloy grains contain various Hf-Al-O-, Hf-O- and Hf-S-rich nano-dispersoids, as well as γ' L1₂-Ni₃Hf nano-precipitates, reflecting reaction of HfO₂ dispersoids in the melt. At the meso-scale, Hf-Al-O-rich slag inclusions are embedded in the metallic matrix, exhibiting a two-phase HfO₂-Al₂O₃ eutectic structure. At the macroscale, millimeter-long cracks form at the boundaries of the elongated, highly (100) textured grains, indicative of solidification cracking. The critical role of Al and O in the superalloy melt in reacting with oxide nano-dispersoids during PBF-LB manufacturing, previously reported for Y₂O₃ nano-dispersoids, is observed to occur here for HfO₂ dispersoids as well, despite their higher stability, melting point and density and their lack of reactivity with Al₂O₃.

1. Introduction

Oxide-dispersion-strengthened (ODS) nickel-base superalloys contain low volume fraction of nanometric, coarsening-resistant oxide dispersoids which strengthen the metallic matrix, at ambient and elevated temperatures, together with high volume fractions of larger γ' precipitates formed during aging [1]. ODS superalloys are usually produced in simple billet shapes via powder metallurgy methods: sintering, hot (isostatic) pressing and spark plasma sintering (SPS) [1–5]. The low machinability of these highly-reinforced superalloys motivates research in additive manufacturing as an alternative fabrication method, in particular via rapid melting and solidification through laser-based powder-bed fusion (PBF-LB). This processing through the liquid state of the metallic alloy, unlike the traditional solid-state powder metallurgy approaches, brings new opportunities (e.g., larger alloy grains with low segregation and high solidification texture desirable for creep resistance) as well as new challenges associated with the very high temperatures reached in the melt pool, (e.g., melting, dissolution, decomposition and/or reactions of the solid oxide dispersoids, which is exacerbated by their very small sizes) [6,7].

Recently, we investigated PBF-LB processing of a Ni-8Cr-5.5Al-1Ti (wt%) model superalloy with and without 0.5–1 wt% Y₂O₃ nano-dispersoids additions [6,7]. This simple quaternary superalloy exhibits Cr, Al and Ti concentrations similar to those of the commercial Ni-base superalloy CM247LC, which provide high volume fractions of γ' precipitates on aging. This simple composition allowed for a basic assessment of the interaction of Y₂O₃ dispersoids with the main reactive elements (Cr, Al and Ti) of this class of alloys in the molten state. Y₂O₃ nanoparticles were incorporated into the alloy grains, inducing a strong (100) texture, and noticeably reducing grain size, as compared to the unmodified base alloy [6,7]. Also, the addition of 0.5 wt% Y₂O₃ nano-dispersoids noticeably improved the creep resistance of the Ni-8Cr-5.5Al-1Ti alloy, after aging to form γ' precipitates [8,9]. However, some of the Y₂O₃ nano-dispersoids were consumed by reaction with Al₂O₃ (most likely from the alloy powder surface) to form Y₄Al₂O₉ slag, incorporated in the solid alloy as horizontally aligned lenses [6,7]. Further loss of Y₂O₃ particles occurred by thermal decomposition in the melt pool, as inferred from the presence of Ni- and Y-rich nanoparticles in the solidified alloy and from Y segregation to the grain boundaries, resulting in embrittlement [6,7].

* Corresponding author at: Empa – Swiss Federal Laboratories for Materials Science and Technology, Überlandstrasse 129, Dübendorf 8600, Switzerland.
E-mail address: christian.leinenbach@empa.ch (C. Leinenbach).

¹ These authors contributed equally to this work.

² Current address: ABB Research Center, Segelhofstrasse 30–34, 5405 Baden, Switzerland

Table 1

Measured composition and impurity elements in the base powder. O, C and S are determined by melt combustion after ASTM E1019–18, rest by ICP-OES after ASTM E1479–16 through a commercial testing lab.

	Ni	Cr	Al	Ti	Co	Fe	Cu	Si	C	Zr	Hf	B	S	O
			(wt.%)							(wt.ppm)				
Ni-Cr-Al-Ti	Bal	8.76	5.39	1.17	0.10	140	90	120	80	<10	<10	<10	50	220

The reaction between added Y_2O_3 nano-dispersoids and native Al_2O_3 lead to the hypothesis that optimal dispersoids should be unreactive with Al_2O_3 [6,7]. A survey of high-melting binary oxides revealed that most form ternary oxides with Al_2O_3 (e.g., $2Y_2O_3 + Al_2O_3 = Y_4Al_2O_9$) [6,7,10–15], with the exception of two high-melting oxides, ZrO_2 and HfO_2 [13,15] which were thus identified as dispersoid candidates to replace Y_2O_3 in Al-rich Ni-base superalloys [6,7]. In fact, HfO_2 was successfully added by laser-directed energy deposition to oxide-dispersion strengthened (ODS) steels, which however lacks the high-reactivity, high-oxide-forming Cr, Al and Ti elements present in Ni-base superalloys [16]. Also, as compared to Y_2O_3 and ZrO_2 , HfO_2 has a much higher density (9.7 vs. 5.0 and 5.7 g/cm³ respectively) and it is denser than the liquid alloy (~ 7.3 g/cm³), thus potentially reducing buoyancy-induced surface agglomeration and slag formation: while the lighter Y_2O_3 (and ZrO_2) nanoparticles can float and agglomerate into large slag regions at the surface of the traveling liquid melt pool, the heavier HfO_2 particles may be expected to sink and be incorporated in the solidifying melt.

The goal of the present study is to investigate the above hypothesis [6,7] that HfO_2 can successfully replace Y_2O_3 as nano-dispersoid additions during the PBF-LB processing of ODS Ni-base alloys with high Al content, based on (i) the lack of ternary compound formation between HfO_2 and Al_2O_3 , (ii) the high density of HfO_2 , and (iii) its excellent chemical stability, reflected in its very high melting point of 2758 °C. Using various microscopy methods, we ascertain the evolution of HfO_2 nano-dispersoids after the very rapid melting, superheating, and solidification of HfO_2 -containing Ni-8Cr-5.5Al-1Ti (wt%) powders occurring during PBF-LB processing, and we compare the fate of these HfO_2 nano-dispersoids to previously reported Y_2O_3 nano-dispersoids.

2. Experimental procedures

Prealloyed Ni-8.5Cr-5.5Al-1Ti (wt%) powders were fabricated by Nanoval (Germany) by gas-atomization and sieved to 63 μ m. The powder also contains trace amounts of C, Si, O, and S, with the chemical analysis reported in Table 1. The HfO_2 -modified powders were produced by rotational ball milling for 24 h of these prealloyed powders together with 0.96 wt% HfO_2 nanoparticles (60–80 nm, 99.99%, US Research Nanomaterials), using polypropylene vials with ZrO_2 media (5:1 ball-to-powder ratio), which could potentially trace amount of Zr into the alloy, as previously observed in previous works [7], at levels below <100 wt.ppm.

Powders were melted and solidified into $5 \times 5 \times 5$ mm³ cubic specimens in a Sisma MySint 100 (Sisma S.p.A., Italy) laser-based powder-bed fusion instrument equipped with a 200 W fiber-laser operating in continuous-wave mode (with 55 μ m spot size and 1070 nm wavelength) under Ar shielding gas ($O_2 < 0.01\%$). A bidirectional scan strategy (90° rotation between layers) was used for each layer, followed by a contour scan, with layer thickness $t = 30$ μ m and hatch spacing $h = 75$ μ m. For each specimen, a different combination of power ($P = 125$ – 175 W) and scanning speed ($v = 750$ – 1250 mm/s) was used, leading to a range of volumetric energy densities $E = P/(v \cdot h \cdot t)$. These parameters were selected to allow direct comparison with previous works on the model alloy as well as a 0.5 wt% Y_2O_3 modified variant [6,7], whose dispersoid volume fraction is similar to 0.96 wt% HfO_2 .

The density of the manufactured cubes was measured in ethanol by the Archimedes method. The cubes were then mounted in epoxy,

ground, and polished with 3–1 μ m diamond suspensions, with a final step with 50 nm colloidal silica. The cubes were oriented to reveal the x-z plane (where z is the build direction). A complete microstructural characterization was conducted on a cube manufactured with a laser power of 150 W and a scan speed of 1000 mm/s. Argon-ion beam polishing (Leica TIC) was used for surface preparation to map grain orientation by electron backscatter diffraction (EBSD), performed at a step size of 2 μ m at 30 kV acceleration voltage on a JEOL 4700F FIB-SEM with a Symmetry S2 (Oxford Instruments) detector.

Crack density was estimated from the analysis of full vertical cross-sections from images provided in Supplementary Fig. 3. For each sample, about 300 images (at 200x magnification, acquired and stitched using a Leica VZ700C optical microscope) were analyzed using the ‘analyze particles’ function from ImageJ. The images were median-filtered followed by manual thresholding and binarization. Particles were filtered out if they were smaller than 20 pixels, touched edges, or had a circularity above 0.35 (pores). Additionally, vertically elongated slag particles were manually removed. To obtain crack length, visible cracks were fitted by ellipses.

The phase transformation temperatures of the HfO_2 -modified alloy were determined by differential scanning calorimetry (DSC) measurements (NETZSCH DSC 404C Pegasus). A sample of 25.5 mg was used. To ensure better thermal conduction with the Al_2O_3 crucible, the sample's surfaces were grinded with SiC grinding paper to P4000. The experiments were carried out under high-purity Ar atmosphere (99.9999% Ar) with a flow rate of 40 ml/min. The crucibles were heated at a rate of 10 K/min from 20 to 1430 °C and cooled at the same rate. Only the heating thermograms are considered in this study and compared with data from the base alloy without oxide additive (from Ref. [6]).

A transmission electron microscopy (TEM) lamella was extracted perpendicular to the build direction using a FEI Helios NanoLab 600i focused ion beam (FIB). Scanning transmission electron microscopy (STEM) was conducted at 300 kV on a FEI Titan Themis microscope, equipped with a probe spherical aberration corrector. The SuperEDX system (ChemiSTEM technology), with four silicon drift detectors, was used for energy-dispersive X-ray (EDX) spectroscopy and mapping. A convergence semi-angle of 25 mrad was used in combination with an annular dark field (ADF) detector with inner and outer collection semi-angles of 53 and 200 mrad, respectively.

The EBSD data analysis was performed in AztecCrystal (Oxford Instruments, UK) and semi-quantitative EDS data processing employed Velox 3.0. Data visualization was performed in Python (Anaconda, Continuum Analytics).

3. Results and discussion

The HfO_2 modification of the model Ni-Cr-Al-Ti alloy had a noticeable effect on the surface quality of the cubes, Supplementary Fig. 1. The HfO_2 -free base alloy cubes have relatively rough top surfaces (with deep valleys and local build-up), whereas the HfO_2 -modified cubes exhibit very flat top surfaces with limited build-up (only localized closer to the contour), consistent with the formation of more stable and reproducible melt tracks. This process stability is further highlighted by the density curve presented in Fig. 1a, where the HfO_2 -modified alloy shows a near constant density plateau between 50 to ~ 105 J/mm³, albeit at a lower density value than the base alloy. The DSC measurements reveal noticeable changes in the alloy, Supplementary Fig. 2. In the HfO_2 -modified

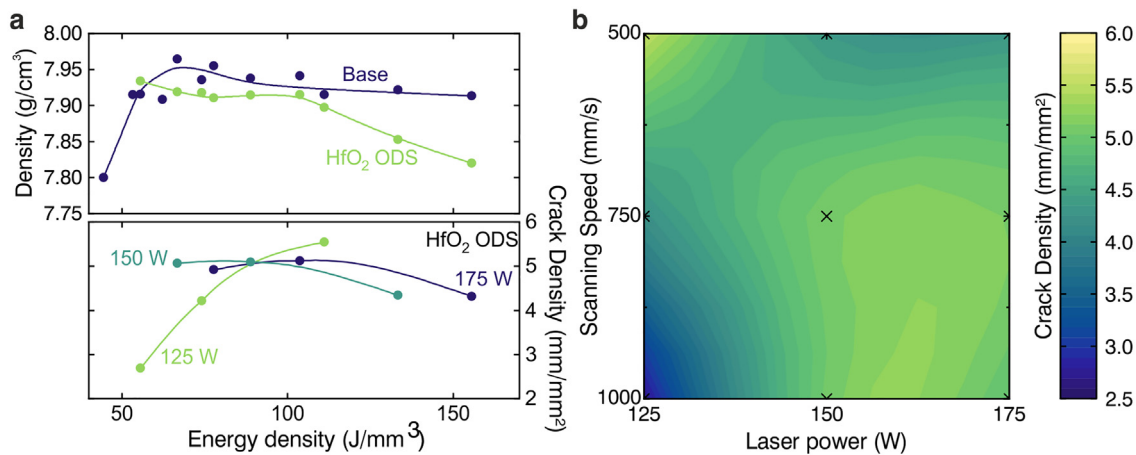


Fig. 1. – (a) Volumetric density and crack density of solidified HfO₂-modified alloy as a function of laser energy density (values for the HfO₂-free base alloy are from Ref. [6]); (b) crack density map for HfO₂-modified alloy, interpolated from various combinations of scanning speeds and laser power.

alloy, the γ' solvus temperature is increased by ~ 8 °C (1119 °C) and the solidus temperature is slightly decreased by 4 °C (1377 °C), with the melting onset ~ 20 °C lower (1350 °C). These changes suggest reaction of the HfO₂-dispersoids with the molten alloy. By contrast, the liquidus temperature is unchanged, within experimental error (1404 °C).

Microstructure investigations of the HfO₂-modified alloy reveal the presence of a high number of defects: gas pores from keyhole formation (limited to part consolidated at high energy densities above ~ 110 J/mm³ with scan speed of 500 mm/s), slag inclusions and cracks (Supplementary Fig. 3). A fraction of the porosity originates from the raw powder, as highlighted by the work on the HfO₂-free alloy [6]. The same alloy modified with Y₂O₃-dispersoids [6,7] also suffered from those defects (Al₂O₃ or Y₄Al₂O₉ slag lenses, low-to-medium number density cracks), their occurrence level in the present HfO₂-modified alloy is much higher and more pronounced, e.g., cracks extend vertically over 1 mm. Similarly to the base- and Y₂O₃-modified alloys [6,7], the slag fraction decreases with increasing energy density, while the crack density shows the opposite trend, Fig. 1. The laser power has a noticeable effect on crack density, as evidenced by the crossing of the curves when plotted against energy density. The slag fraction could not be quantitatively estimated from the cross-section imaging and is thus not included.

Also, as shown in Fig. 1a, a sharp decrease in volumetric density is observed for energy densities above 105 J/mm³, suggesting a change in consolidation behavior. Cross-sectional imaging reveals a drastic increase in porosity for these samples, consistent with deep-keyhole porosity. Interestingly, while lack-of-fusion defects in the base alloy were never completely prevented within the investigated parameter field, the observation of such defects was very rare in the HfO₂-modified alloy.

Further in-depth investigations were focused on a sample printed with a single combination of power (150 W) and scan speed (1000 mm/s). Three types of defects are observed, Fig. 2: (i) spherical gas porosity, (ii) cracks and (iii) slag inclusions. Spherical pores, with median diameters of ~ 2 μ m, and only a few reaching above 10 μ m (max ~ 25 μ m), are randomly distributed in the specimen for this printing condition; they are expected to be due to entrapped gas porosity in the powder, as previously reported for the unmodified alloy [6].

The near-vertical cracks propagate inter-granularly between grains located close to melt pool boundaries and they are often observed with horizontal spacings of ~ 75 μ m, matching the hatch distance. Unlike in the base- and Y₂O₃-modified alloys [6,7] which exhibit brittle cracking of GBs, the present HfO₂-modified alloy exhibits rough crack surfaces with a structure reminiscent of dendrites, suggesting solidification cracking, Fig. 2e. This type of cracking was also observed in the

Hf-containing CM247LC alloy [17], and result from the interdendritic segregation of Hf which locally lower the alloy's melting point.

The slag particles have complex shapes and are easy to detect by SEM given their sharp Z-contrast provided by Hf enrichment, Fig. 2a,f,g. When embedded in the alloy, the slag particles are found in the center of the melt tracks, often elongated vertically. This observation contrasts those of Al₂O₃ and Y₄Al₂O₉ slag inclusions adopting lens shapes in the base- and Y₂O₃-modified alloys [6,7], which are located on the melt pool top surface, before being incorporated into the matrix when a subsequent layer is deposited. While some surface slag was observed in the present HfO₂-modified alloy, the slag inclusions do not adopt a lens shape; this is consistent with the scenario that molten slag sinks into (rather than float on) the melt pool, based on the slag composition estimated by chemical mapping and line profile, Fig. 2 g, h. The slag is enriched in Hf, Al and O. However, no ternary compounds are given in the Hf-Al-O ternary phase diagram [18], or in the general literature; only a low eutectic point between HfO₂ and Al₂O₃ (31% Al, 1880 °C) and a solubility of ~ 3 mol.% Al in HfO₂ are reported [18]. Closer inspection of the slag inclusions reveals a dendritic microstructure, Fig. 2 g; BSE contrast suggests that the slag dendritic and interdendritic regions are enriched in Hf and Al, respectively. The slag is thus more likely a eutectic network of HfO₂ and Al₂O₃, which average composition leads to an atomic ratio close to Hf:Al:O of $\sim 2:1:5$ within the slag. Nonetheless, the observation of a Hf-Al-rich slag reveals that the HfO₂ nano-dispersoids (despite their very high melting point of 2758 °C) agglomerated and reacted with the molten alloy to form a high-temperature ionic melt. Additionally, stringers of interdendritic submicron particles are observed within the grains and at grain boundaries, Fig. 2d. Despite the high slag fraction and high crack density, slag inclusions were extremely rarely found to interact with cracks.

EBSD maps for the HfO₂-modified alloy shows columnar grains spanning up to 25–30 deposition layers oriented along the build direction, indicating some degree of epitaxy during the solidification of subsequent layers (Fig. 3a). Most of the grains show alignment of their (100) direction with all the major axes of the PBF-LB process, the build direction z and the two perpendicular scan axes x and y (Fig. 3b). However, some grains also exhibit (110) and (111) aligned with the build directions (green and blue shades in Fig. 3a). This indicates a competition of energetically-favorable 100 texture and the 110 and 111 grain populations typically associated with higher energy input and longer melt pool lifetimes. This strong texture observation is in stark contrast with the microstructure of the base material, which showed weak texture despite its very elongated grain structure [6]. However, as in the HfO₂-modified alloy, the same increased texture was observed in the Y₂O₃-modified

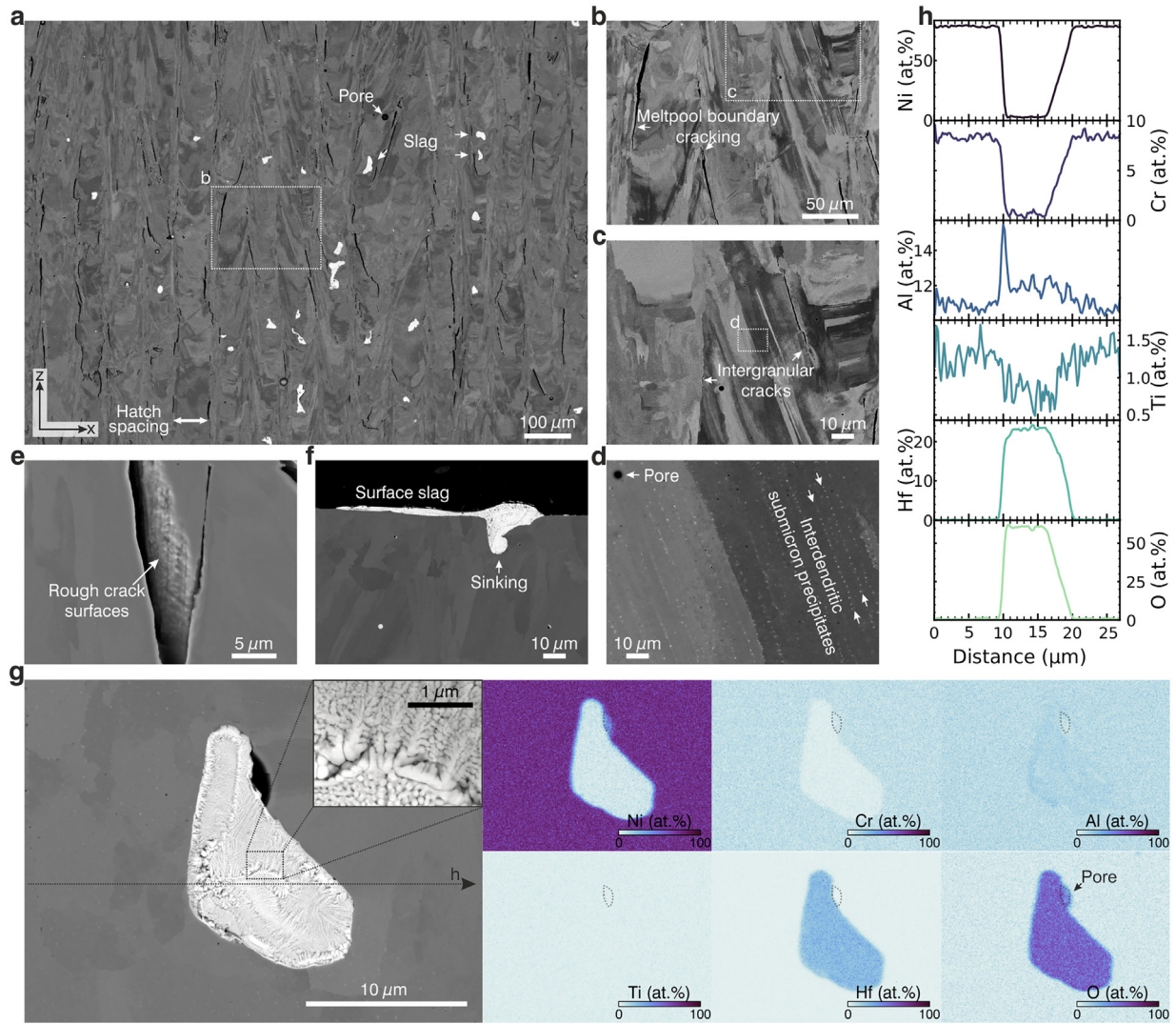


Fig. 2. Microstructure of HfO₂-modified alloy ($P = 150$ W, $v = 1000$ mm/s). (a–f) SEM micrographs of a vertical cross-section, show a very elongated grain structure, regularly spaced cracks, micropores, and vertically-elongated globular slag inclusions. The cracks are located at the melt-pool boundaries, and more particularly propagate along grain boundaries; the crack surfaces appear dendritic, suggesting solidification cracking. Submicron particles rich in heavy elements populate the interdendritic regions. (g–h) EDS mapping and line of a ~ 10 μ m-wide slag particle with an average compositional Hf:Al:O atomic ratio close to 2:1:5. A higher magnification micrograph in the inset highlights the submicron dendritic structure of the slag inclusion.

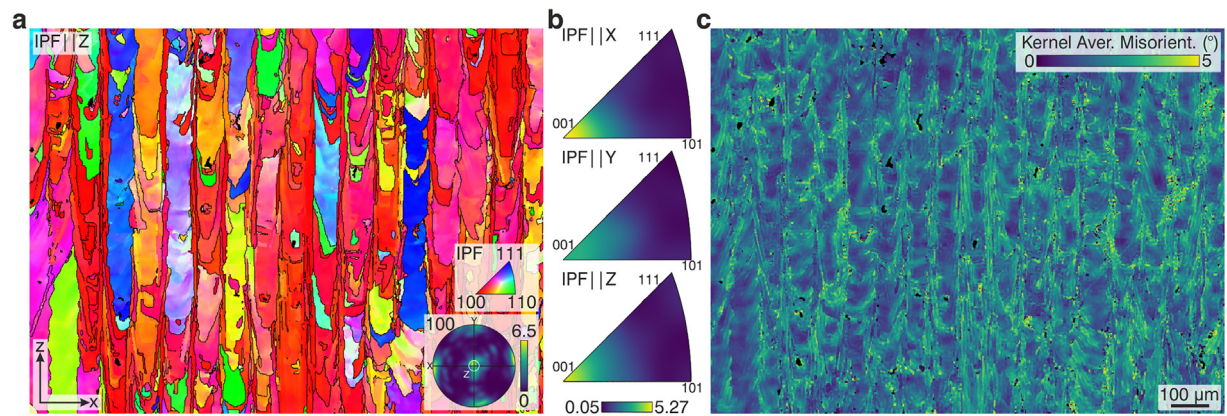


Fig. 3. EBSD maps of HfO₂-modified alloy ($P = 150$ W, $v = 1000$ mm/s). (a) Inverse pole figure colored map along the build direction z. (b) Inverse pole figure maps, along the build direction z and the transverse x and y directions, show strong alignment of 001 with the build and transverse directions. (c) Kernel average misorientation map, highlighting the residual strain in the grains and along grain boundaries. The EBSD maps cover the same zone shown in Fig. 2a and the scale bar in (c) is valid for both maps.

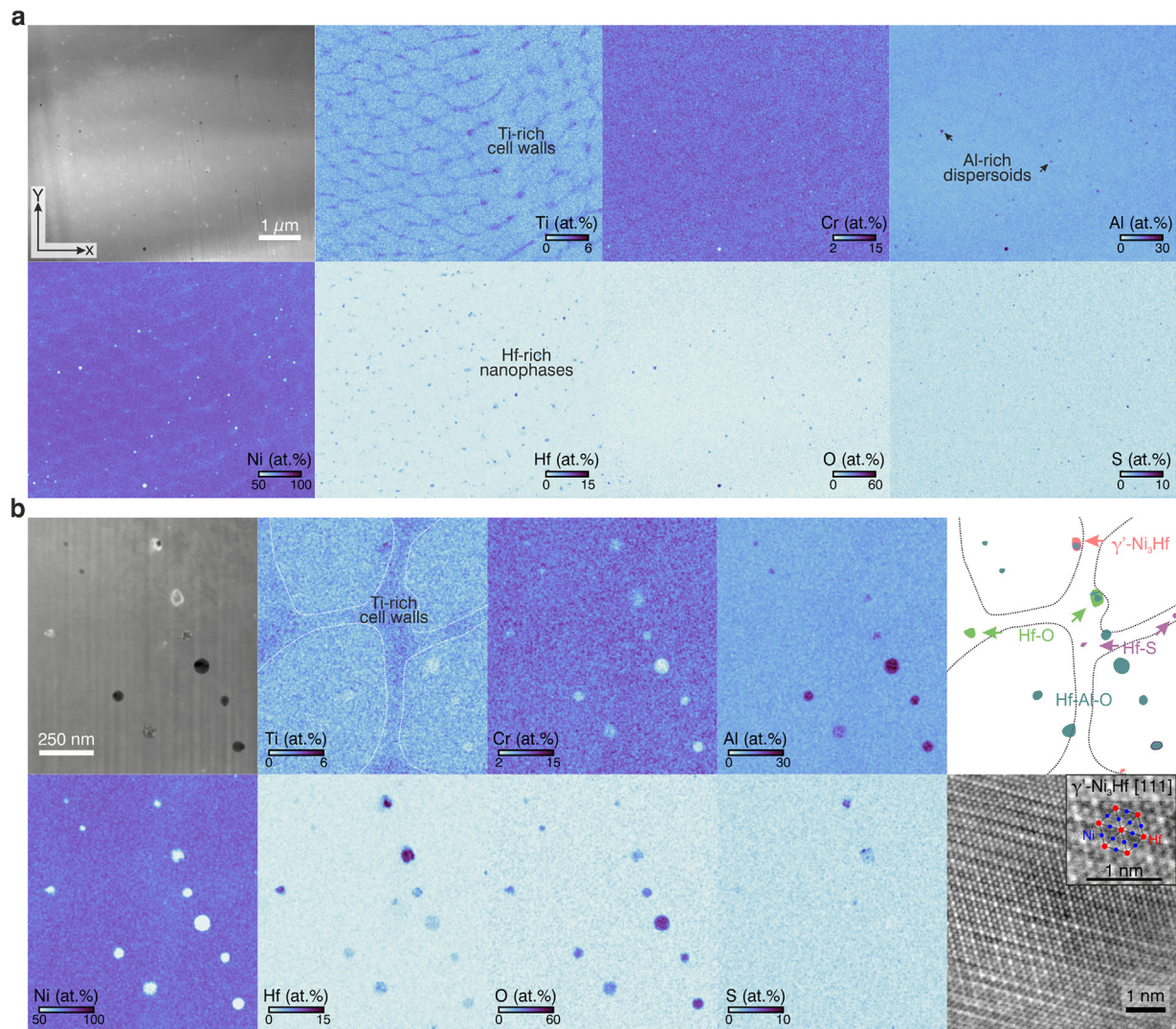


Fig. 4. Chemical distribution in HfO₂-modified alloy ($P = 150$ W, $v = 1000$ mm/s). TEM EDS map reveals the fine microstructure of the alloy. a) The dendrite cell regions are marked by an increased Ti segregation. A high number density of Hf-rich nanophases are observed, more often located in the interdendritic regions, suggesting a rejection by the solidification front. b) Multiple types of Hf-rich nanophases are identified and labeled as Hf-O, Hf-Al-O and Hf-S. High-resolution imaging (bottom-right pane) reveals that the Hf-rich nanophase exhibits a γ' L1₂-Ni₃Hf crystal structure, as observed here along its [111] zone axis.

Ni-Cr-Al-Ti alloy [7]. It was hypothesized that the nanodispersoid rejection rate by the solidification front depends on the dendrite's crystal orientation. In that regard, the 100 direction perpendicular to the planar solidification front is then growing the fastest, with the nanodispersoids acting as seed selectors. Comparing EBSD maps and BSE-SEM micrographs (Fig. 2) reveals that, while the alloy consists of very long grains separated by high-angle grain boundaries, the grains contain a high density of small-angle grain boundaries leading to contrast in BSE. The kernel average misorientation map (Fig. 3c) shows that these small-angle grain boundaries are predominantly located near the former melt pool boundaries, indicating stress concentration in these areas, which is consistent with the observed formation of cracks.

TEM investigation reveals the fine microstructure of the HfO₂-modified alloy, Fig. 4. As in the HfO₂-free base alloy [6], strong Ti interdendritic segregation marks the position of the solidification cells walls. A relatively high number of Hf/Al/O/S-rich nano-particles are found distributed through the matrix, with an increased occurrence within, or close to, the solidification cell walls, suggesting rejections in the still liquid metal during solidification. Four types of nanoparticles are observed (Fig. 4b), all rich in Hf: Hf-Al-O-rich (dark) dispersoids, and Hf-O- and Hf-S-rich (bright) dispersoids. The fourth type shows only an increase

in Hf and is identified as γ' L1₂-Ni₃Hf via high-resolution imaging. Interestingly, the scavenging of S contaminant by Hf does not involve the formation of oxy-sulfides as observed in the Y₂O₃-modified alloy [7]. Additionally, the reaction between Ti and S observed in the base alloy is prevented [6]. This confirms the S-scavenging role of Hf in nickel alloys [19,20].

4. Conclusions

To investigate the incorporation and stability of HfO₂ dispersoids in high- γ' nickel-base superalloys processed by laser-based powder-bed fusion (PBF-LB), powders of a simplified Ni-8.5Cr-5.5Al-1Ti (wt%) model alloy were ball-milled with 0.96 wt% HfO₂ nano-powder and subjected to laser fusion and subsequent rapid solidification.

Defect formation follow the same trends previously observed in a Ni-Cr-Al-Ti base alloy free of HfO₂ particles: increasing laser energy density reduces slag incorporation, but also increases cracking.

Specifically, the addition of HfO₂ nanoparticles to the alloy leads to:

- (i) A high number density of cracks, likely linked to the formation of Hf-rich regions along grain boundaries and solidification cracking;

- (ii) Numerous Hf-Al-O-rich slag inclusions, showing a two-phase structure consistent with the $\text{HfO}_2\text{-Al}_2\text{O}_3$ eutectic;
- (iii) Various Hf-rich nano-dispersoids indicating extensive reaction of HfO_2 dispersoids in the melt: Hf-Al-O-, Hf-O- and Hf-S-rich precipitates, as well γ' $\text{L}_{12}\text{-Ni}_3\text{Hf}$ precipitates;
- (iv) Absence of oxy-sulfides (as observed in the Y_2O_3 -modified alloy) and titanium sulfide (as observed in the base alloy), illustrating the strong S-scavenging ability of Hf;
- (v) A strong enhancement of the (100) alloy's texture.

The lack of stability of HfO_2 during PBF-LB processing, which leads to Hf dissolution into the molten alloy and formation of undesirable phases, challenge the use of HfO_2 as a viable dispersoid choice for Al-rich nickel superalloys.

Declaration of Competing Interest

The authors declare that they have no known competing financial interests or personal relationships that could have appeared to influence the work reported in this paper.

Data availability

Data will be made available on request.

Acknowledgments

The research leading to this work was funded by the US Army Research Office (W911NF-18-1-0129). Electron microscopy was performed at Northwestern's NUANCE center which receives support from the MRSEC program (NSF DMR-1720139) at the Materials Research Center and the SHyNE Resource (NSF ECCS-1542205). This work made use of the MatCI Facility which receives support from the MRSEC Program (NSF DMR-1720139) of the Materials Research Center at Northwestern University.

Supplementary materials

Supplementary material associated with this article can be found, in the online version, at [doi:10.1016/j.addlet.2023.100139](https://doi.org/10.1016/j.addlet.2023.100139).

References

- [1] G.H. Gessinger, Chapter 7 - Oxide-dispersion-strengthened superalloys, in: *Powder Metallurgy of Superalloys*, Butterworth-Heinemann, 1984, pp. 213–292, [doi:10.1016/B978-0-408-11033-4.50014-2](https://doi.org/10.1016/B978-0-408-11033-4.50014-2).
- [2] W. Chen, W. Xiong, X. Zhang, Effect of Y_2O_3 content and sintering temperature on mechanical properties of ODS nickel-based superalloy, *Rare Met. Mater. Eng.* 39 (2010) 112–116.
- [3] J. Jang, T.K. Kim, C.H. Han, H.K. Min, S.H. Jeong, D.H. Kim, A preliminary development and characterization of Ni-based ODS alloys, *Proced. Eng.* 55 (2013) 284–288, [doi:10.1016/j.proeng.2013.03.255](https://doi.org/10.1016/j.proeng.2013.03.255).
- [4] T. Kong, B. Kang, H.J. Ryu, S.H. Hong, Microstructures and enhanced mechanical properties of an oxide dispersion-strengthened Ni-rich high entropy superalloy fabricated by a powder metallurgical process, *J. Alloys Compd.* 839 (2020) 155724, [doi:10.1016/j.jallcom.2020.155724](https://doi.org/10.1016/j.jallcom.2020.155724).
- [5] L. Yu, Z. Lu, S. Peng, X. Li, Effect of Al/Ti ratio on γ' and oxide dispersion strengthening in Ni-based ODS superalloys, *Mater. Sci. Eng. A* 845 (2022) 143240, [doi:10.1016/j.msea.2022.143240](https://doi.org/10.1016/j.msea.2022.143240).
- [6] A. De Luca, C. Kenel, S. Griffiths, S.S. Joglekar, C. Leinenbach, D.C. Dunand, Microstructure and defects in a Ni-Cr-Al-Ti γ/γ' model superalloy processed by laser powder bed fusion, *Mater. Des.* 201 (2021) 109531, [doi:10.1016/j.matdes.2021.109531](https://doi.org/10.1016/j.matdes.2021.109531).
- [7] C. Kenel, A. De Luca, S.S. Joglekar, C. Leinenbach, D.C. Dunand, Evolution of Y_2O_3 dispersoids during laser powder bed fusion of oxide dispersion strengthened Ni-Cr-Al-Ti γ/γ' superalloy, *Addit. Manuf.* 47 (2021) 102224, [doi:10.1016/j.addma.2021.102224](https://doi.org/10.1016/j.addma.2021.102224).
- [8] C. Kenel, A. De Luca, C. Leinenbach, D.C. Dunand, High-temperature creep properties of an additively manufactured Y_2O_3 oxide dispersion-strengthened Ni-Cr-Al-Ti γ/γ' superalloy, *Adv. Eng. Mater.* 24 (2022) 2200753, [doi:10.1002/adem.202200753](https://doi.org/10.1002/adem.202200753).
- [9] Y.I. Lee, E.S. Lee, S.T. Oh, Effect of Y_2O_3 dispersion method on the microstructure characteristic of ni-base superalloy, *J. Nanosci. Nanotechnol.* 21 (2021) 4955–4958, [doi:10.1166/jnn.2021.19253](https://doi.org/10.1166/jnn.2021.19253).
- [10] H.v. Wartenberg, H.J. Reusch, Schmelzdiagramme höchstfeuerfester Oxyde. IV. (Aluminiumoxyd), *Z. Anorg. Allgem. Chem.* 207 (1932) 1–20, [doi:10.1002/zaac.19322070102](https://doi.org/10.1002/zaac.19322070102).
- [11] P. Wu, A.D. Pelton, Coupled thermodynamic-phase diagram assessment of the rare earth oxide-aluminum oxide binary systems, *J. Alloys Compd.* 179 (1992) 259–287, [doi:10.1016/0925-8388\(92\)90227-Z](https://doi.org/10.1016/0925-8388(92)90227-Z).
- [12] R.S. Roth, J.R. Dennis, H.F. McMurdie, Phase equilibria diagrams: phase diagrams for ceramics, *Am. Ceram. Soc.* (1995) 107.
- [13] S. Lakiza, O. Fabrichnaya, M. Zinkevich, F. Aldinger, On the phase relations in the $\text{ZrO}_2\text{-YO}_{1.5}\text{-AlO}_{1.5}$ system, *J. Alloys Compd.* 420 (2006) 237–245, [doi:10.1016/j.jallcom.2005.09.079](https://doi.org/10.1016/j.jallcom.2005.09.079).
- [14] P. Villars, H. Okamoto, Al-O-Sc Vertical Section of Ternary Phase Diagram: Datasheet from "PAULING FILE Multinaries Edition – Switzerland & National Institute for Materials Science (NIMS), Springer-Verlag Berlin Heidelberg & Material Phase s Data System (MPDS), Japan, 2012.
- [15] Z. Cao, W. Xie, Z. Qiao, X. Xing, Thermodynamic modeling of the $\text{HfO}_2\text{-La}_2\text{O}_3\text{-Al}_2\text{O}_3$ system, *J. Am. Ceram. Soc.* 100 (2017) 365–377, [doi:10.1111/jace.14462](https://doi.org/10.1111/jace.14462).
- [16] B.M. Arkhurst, J.J. Park, C.H. Lee, J.H. Kim, Direct laser deposition of 14Cr oxide dispersion strengthened steel powders using Y_2O_3 and HfO_2 dispersoids, *Korean J. Met. Mater.* 55 (2017) 550–558, [doi:10.3365/KJMM.2017.55.8.550](https://doi.org/10.3365/KJMM.2017.55.8.550).
- [17] S. Griffiths, H. Ghasemi Tabasi, T. Ivas, X. Maeder, A. De Luca, K. Zweier, R. Wróbel, J. Jhabvala, R.E. Logé, C. Leinenbach, Combining alloy and process modification for micro-crack mitigation in an additively manufactured Ni-base superalloy, *Addit. Manuf.* 36 (2020) 101443, [doi:10.1016/j.addma.2020.101443](https://doi.org/10.1016/j.addma.2020.101443).
- [18] L.M. Lopato, A.V. Shevchenko, G.I. Gerasimiyuk, The system $\text{HfO}_2\text{-Al}_2\text{O}_3$, *Inorg. Mater.* 12 (1976) 1331–1334.
- [19] C. Sarioglu, C. Stinner, J.R. Blanchere, N. Birks, F.S. Pettit, G.H. Meier, The control of sulfur content in nickel-base, single crystal superalloys and its effect on cyclic oxidation resistance, *Superalloys 96* (1996) 71–80.
- [20] R.W. Jackson, D.M. Lipkin, T.M. Pollock, The oxidation and rumpling behavior of overlay B2 bond coats containing Pt, Pd, Cr and Hf, *Surf. Coat. Technol.* 221 (2013) 13–21, [doi:10.1016/j.surfcoat.2013.01.021](https://doi.org/10.1016/j.surfcoat.2013.01.021).